

All-Solid-State Electro-Chemo-Mechanical Actuator Operating at Room Temperature

Evgeniy Makagon, Ellen Wachtel, Lothar Houben, Sidney R. Cohen, Yuanyuan Li, Junying Li, Anatoly I. Frenkel, and Igor Lubomirsky*

Dimensional change in a solid due to electrochemically driven compositional change is termed electro-chemo-mechanical (ECM) coupling. This effect causes mechanical instability in Li-ion batteries and solid oxide fuel cells. Nevertheless, it can generate considerable force and deformation, making it attractive for mechanical actuation. Here a Si-compatible ECM actuator in the form of a 2 mm diameter membrane is demonstrated. Actuation results from oxygen ion transfer between two 0.1 μm thick Ti oxide/Ce_{0.8}Gd_{0.2}O_{1.9} nanocomposite layers separated by a 1.5 μm thick Ce_{0.8}Gd_{0.2}O_{1.9} solid electrolyte. The chemical reaction responsible for stress generation is electrochemical oxidation/reduction in the composites. Under ambient conditions, application of 5 V DC produces actuator response within seconds, generating vertical displacement of several μm with calculated stress ≈ 3.5 MPa. The membrane actuator preserves its final mechanical state for more than 1 h following voltage removal. These characteristics uniquely suit ECM actuators for room temperature applications in Si-integrated microelectromechanical systems.

fully compatible with Si-based microfabrication techniques.^[3,4] A broad range of emerging micro-electro-mechanical systems (MEMS) do not require efficient energy conversion nor rapid response; however, Si-compatibility combined with fine control over strain (displacement), and stress (force) are sought-after properties.

In 2017, Swallow et al.^[5] proposed a new actuation method. These authors noted that electro-chemo-mechanical (ECM) coupling,^[6–8] namely, mechanical deformation induced by electrochemically driven changes in chemical composition, can be used as an actuation mechanism. ECM coupling is a well-known phenomenon.^[7–10] For example, electrodes of rechargeable batteries undergo repetitive electric current-driven changes in composition accompanied by change in volume, which is one

1. Introduction

Electromechanically active ceramic materials, piezoelectrics^[1] and electrostrictors,^[2] provide the backbone of a variety of important consumer technologies, which include such disparate items as focusing elements in cellular phone cameras and fuel injectors in automobiles. Although piezoelectrics and electrostrictors benefit from a mature technology, emerging regulations, and restrictions on toxic Pb-based components drives the search for new methods to produce electromechanical response. This search is particularly intensive for materials and actuation methods that are, in contrast to Pb-based materials,

of the principal sources of eventual battery failure. In theory, positive or negative strain in a body experiencing an ECM effect can reach a few percent before mechanical failure.^[5,7,8,11–14] Thus, ECM actuation may have the potential to be competitive with piezoelectrics or electrostrictors. To demonstrate ECM actuation, Swallow et al.^[5] electrochemically pumped oxygen into, and out of, a non-stoichiometric Ce_{0.9}Pr_{0.1}O_{1.95– δ} film (δ is oxygen deficiency) deposited on yttria-stabilized zirconia. At 550 °C, out-of-plane, nm-scale displacements were achieved with response time of tens of seconds, which was sufficient for proof of principle but not adequate for practical purposes.

Recently, an ECM contribution to the room temperature electromechanical response of an electrostrictive 20 mol% Gd-doped ceria (Gd_{0.2}Ce_{0.8}O_{1.9}, henceforth 20GDC) tethered membrane, sandwiched between two Ti thin film metal contacts, was reported.^[15] The ECM response was attributed to in situ oxidation/reduction reactions producing several-nm thick layers of TiO_{2– δ} ^[16] at the upper and lower interface between the 20GDC electrolyte and the Ti metal contacts according to the reversible reaction: $\text{Ti} + 2\text{O}^- \rightleftharpoons \text{TiO}_{2-\delta}$, where TiO₂ may take either the rutile or anatase phase. The Ti molar volume increases markedly upon oxidation;^[15] however, once formed, the TiO_{2– δ} interfacial layers impede further ion diffusion into the metal contact, permitting only very limited response. Here, we bring to realization a practical application of the ECM concept in a prototype of a Si-integrated, ECM-based membrane actuator specifically designed to provide micron-size displacements, and long-term stability.

E. Makagon, Dr. E. Wachtel, Prof. I. Lubomirsky
 Department of Materials and Interfaces
 Weizmann Institute of Science
 Rehovot 7610001, Israel
 E-mail: Igor.Lubomirsky@weizmann.ac.il

Dr. L. Houben, Dr. S. R. Cohen
 Chemical Research Support Unit
 Weizmann Institute of Science
 Rehovot 7610001, Israel

Dr. Y. Li, J. Li, Prof. A. I. Frenkel
 Department of Materials Science and Chemical Engineering
 Stony Brook University
 Stony Brook, NY 11794, USA

 The ORCID identification number(s) for the author(s) of this article can be found under <https://doi.org/10.1002/adfm.202006712>.

DOI: 10.1002/adfm.202006712

2. Results and Discussion

The design of a self-supported ECM membrane actuator is similar to that of a solid-state battery: an ion conducting (IC) solid electrolyte sandwiched between two mixed ionic/electronic conductors (MIEC) serving as working bodies (WBs). Applying voltage to such a structure (Figure 1a) induces ion transport through the IC electrolyte causing expansion in one WB, while generating contraction in the other. The strain produced in this process depends on the amount of charge transferred through the IC electrolyte, rather than being a function of the applied voltage. The strain induced by ECM coupling is therefore fundamentally different from electromechanical response in electrostrictors and piezoelectrics. If the upper and lower WBs are constructed from the same material(s), then opposing forces will develop due to alternating oxidation/reduction reactions, producing torque, and consequent bending of the membrane. In the following text, and in the online supporting information sections, we characterize in detail the layered structure, distribution of strain, and electrochemical properties of the Si-compatible ECM membrane actuator.

2.1. Choice of Components

The WBs in our ECM actuator design take advantage of oxygen ion transfer in one of the most extensively studied

ionic conductors, 20GDC. 20GDC is compatible with Si-microfabrication procedures,^[15–17] retains some oxygen ion conductivity at room temperature, is non-toxic and displays excellent mechanical stability.^[15] Efficient WB operation requires: a) a large chemical expansion coefficient and b) rapid ion transport, in order for a sufficiently large volume of material to undergo compositional change. Consequently, we have followed the approach adopted for cermet anode supports in solid oxide fuel cells.^[18–20] We deposited nanocrystalline (average particle size ≈ 40 nm) [Ti oxide/20GDC] composite WBs by co-sputtering Ti metal and 20GDC in Ar at room temperature (see Section 4, Experimental Section) (Figure 1a, Section S4 and Figure S3b, Supporting Information). Ti was chosen because it possesses a rare combination of three unique features: a) It can form three different stoichiometric oxides TiO , Ti_2O_3 , and TiO_2 , which can take up or release oxygen. b) In contrast to Cr or Ni,^[16] for example, all oxides of Ti are electronically conductive and, therefore, do not form insulating, blocking layers. c) Cerium titanate forms only at high temperatures (>1000 °C).^[21,22] Therefore, sputtering produces a composite with a highly elaborate interface promoting oxygen transfer, rather than a chemical compound. According to high resolution EDS elemental mapping (Figure 1b), the composition of the WB nanocomposite with optimal performance contains ≈ 43 at% Ti, with 20GDC comprising the remainder. X-ray absorption near edge structure (XANES) measurements

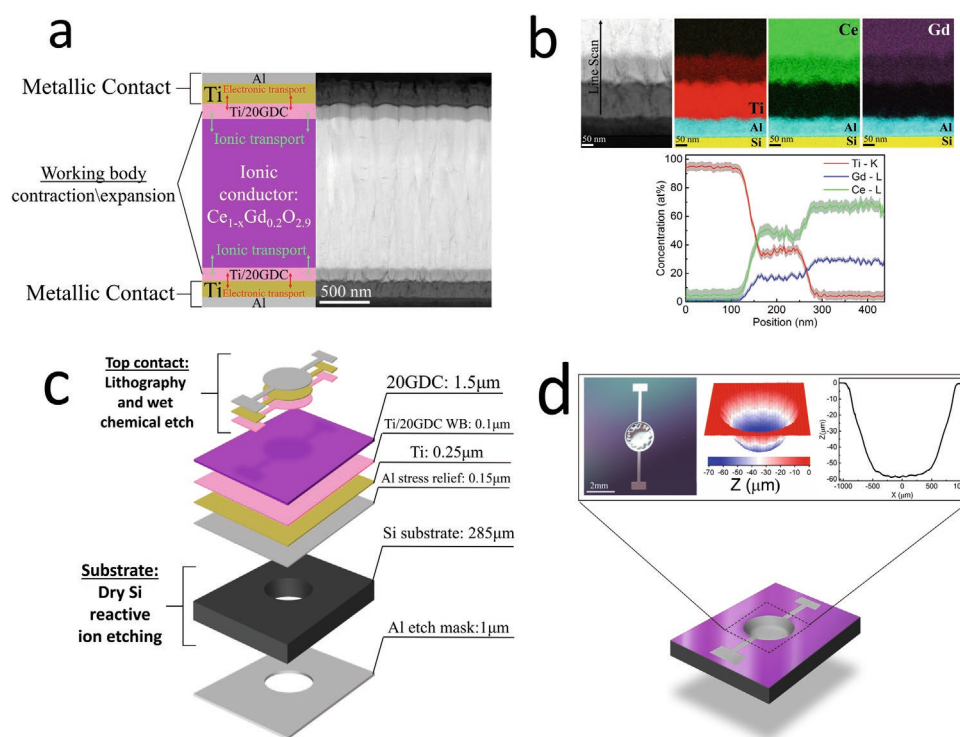


Figure 1. a) Scheme of the ECM actuator showing its basic elements and practical realization. TEM micrograph of a 70–100 nm thick cross section slice of the multilayer stack deposited on a Si substrate (see Section 4, Experimental Section for fabrication details). b) High resolution (1 nm spot size) TEM energy dispersive spectroscopy (EDS) elemental mapping, providing elemental composition of the Si, Al, Ti, WB, and 20GDC solid electrolyte layers. c) Schematic representation of the sputtered layer stack. The structure is transformed into a 2 mm diameter, tethered membrane by means of dry Si etching, lithographic patterning and wet chemical metal etch. d) Image of the membrane buckling pattern and depth profile as measured by an optical profiler (see Section S2, Supporting Information for details).

provide evidence that the WB nanocomposite contains mixed valence states (III and IV) of both titanium and cerium oxides (See Section S1, Supporting Information).

2.2. Actuator Shape and Expected Operation

The ECM-based actuator shown in Figure 1c (see Section 4, Experimental Section for details) is deposited as a thin film stack on a Si wafer with WBs and IC electrolyte as described above. Etching a well in the Si substrate produces 2 mm diameter, tethered, circular membranes. Since even after annealing, the sputtered film stack retains residual in-plane, compressive strain (0.3–0.8%),^[17] the tethered membrane buckles upon substrate removal with buckling depth $\approx 70 \mu\text{m}$ (Figure 1d). The membrane thus assumes the shape of a “soup-bowl” with an almost flat, circular base, $\approx 1 \text{ mm}$ in diameter, surrounded by a petal-like, wrinkled periphery (see Section S2, Supporting Information). AC current-induced mass transfer between the WBs would be expected to impart the following features to the actuator device: i) the large internal surface area of the nanocomposite WB should provide rapid kinetics of both ion transport and charge transfer as compared to rates of transport in bulk materials. ii) Reversing the direction of the electrical current should reverse the direction of the displacement. iii) The amplitude of the response is that of a diffusion driven process, scaling as $1/(\text{frequency})^n$.^[23] iv) Voltage application produces bending, which is consistent with the expansion of one WB while the opposite WB contracts. v) Strain should persist for several hours after removal of DC voltage, since in the absence of mass transfer, strain reduction cannot take place.

2.3. Scanning Probe Microscopy Measurement of Actuator Strain

Application of alternating voltage between the top and bottom electrodes causes the center of the membrane to be displaced vertically, with displacement detected using scanning probe microscope (SPM) (Figure 2a). 20GDC is known to be both anelastic and electrostrictive.^[24–26] Nevertheless, for the actuator

described here, response at the first harmonic was dominant in the frequency range tested ($f = 6 \text{ mHz} - 18.6 \text{ Hz}$). The amplitude of the response ($|\Delta h|$) scales inversely with frequency, f , as:

$$|\Delta h(f)| \propto f^{-0.70 \pm 0.01} \quad (1)$$

which supports a diffusion-driven process (Figure 2b).^[23] The electrochemical reaction responsible for the observed mechanical deformation is attributed to oxidation/reduction in the composite (see Section S3, Supporting Information for details). The ECM actuator is sufficiently robust to be able to operate continuously in this frequency range for 14 h (>2000 cycles at 50 mHz) without measurable degradation in amplitude/structural integrity (see Section S6 and Figure S7, Supporting Information).

We have applied SPM to investigate the variation in displacement across the central region of the membrane actuator in response to application of 8 V, 50 mHz (Figure 3a). In contrast to the electrostrictive response, where this entire region moves in unison due to homogenous expansion of the membrane,^[15,16] here the amplitude $|\Delta h|$ is maximum ($\Delta h_{\text{max}} = 0.43 \pm 0.02 \mu\text{m}$) at the center of that region, while the response at the edge diminishes to $\approx 25\%$ of maximum. The distribution of displacement amplitude is cylindrically symmetric about the membrane center and all positions sampled move in phase. Displacement amplitude can be satisfactorily modeled as a circular arc (Figure 3a, see also Section S2, Supporting Information) with radius of curvature $R_c = 435 \pm 30 \text{ mm}$; this result, along with the symmetry described above, suggests that the membrane under voltage deforms in the form of a spherical dome. As noted above, this is what would be expected if one WB expanded while the other one contracted. With thickness (t) of $1.5 \mu\text{m}$, (Figure S3a, Supporting Information), the stiffness of the 20GDC electrolyte layer must dominate the mechanical response. The average strain (u) may be estimated as^[27]

$$u = \frac{1}{2} t \frac{1}{R_c} = (1.7 \pm 0.1) \times 10^{-6} = 1.7 \text{ ppm} \quad (2)$$

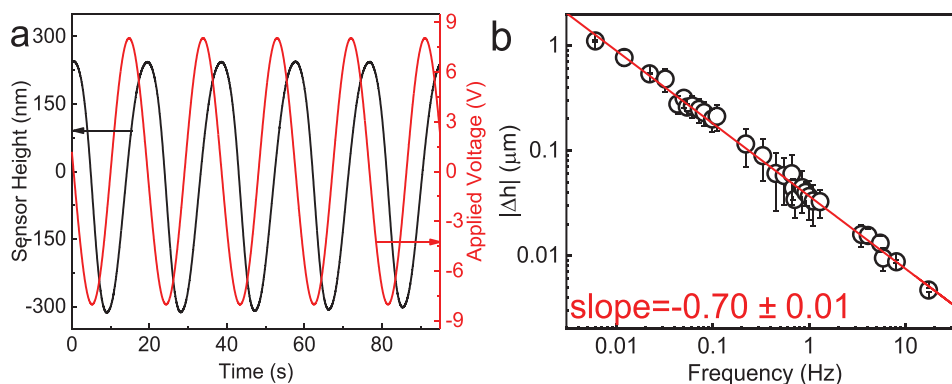


Figure 2. a) Electromechanical response at the center of the actuator measured with a SPM in semi-contact mode. Both the probe and the top contact are at ground potential. The figure shows sensor height as a function of time with 8 V, 50 mHz applied voltage. Baseline was subtracted in order to compensate for thermal drift. b) Log–log plot of the amplitude of ECM response versus bias frequency at 8 V. Six samples were measured and their response averaged. Response amplitude is found to scale inversely with frequency (f) between 6 mHz and 18.6 Hz according to $|\Delta h| \propto f^{-0.7}$ with $R_{\text{adj}}^2 = 0.99807$.

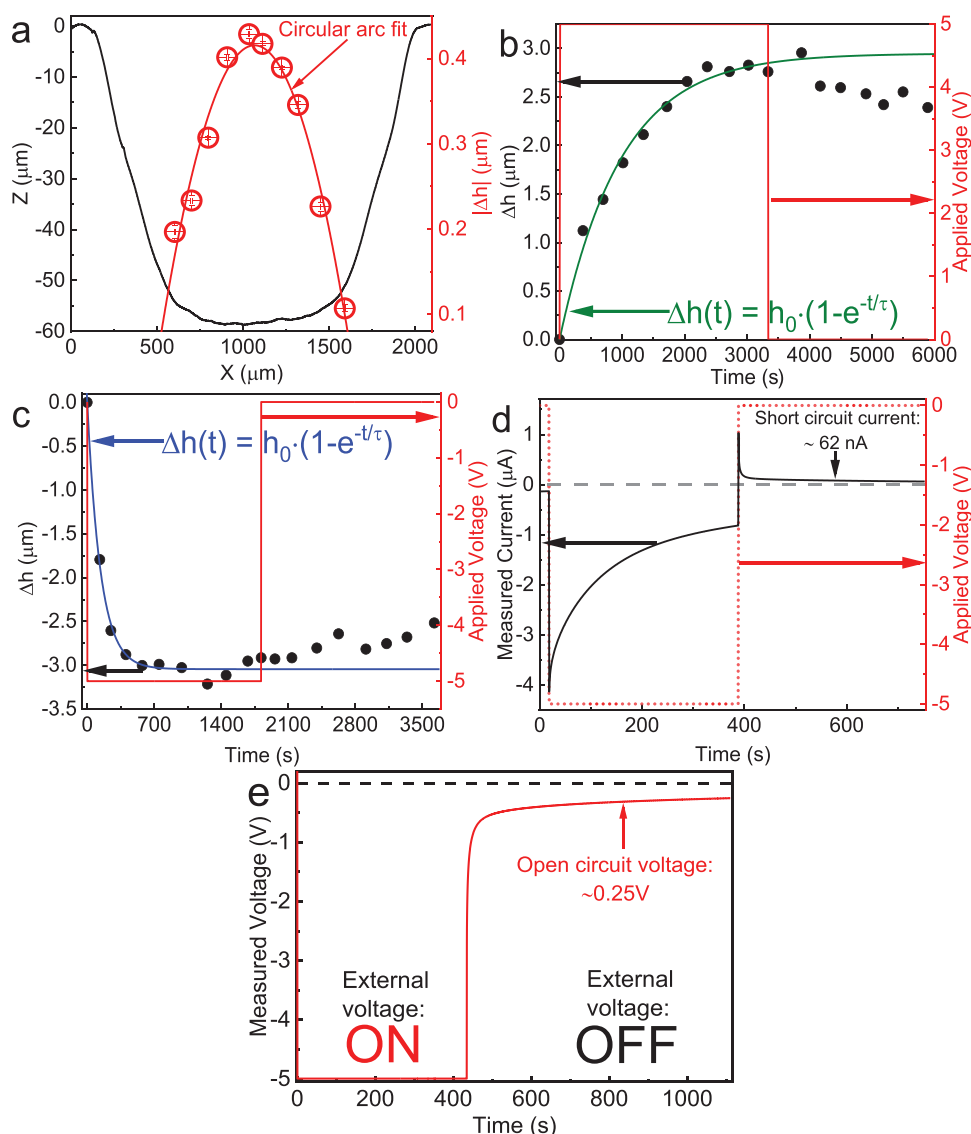


Figure 3. a) (o) The lateral distribution of the amplitude of the electromechanical response ($|\Delta h|$) of the central 1mm diameter region of the membrane to 8 V 50 mHz as measured with the SPM. The microscope tip and top contact were at ground potential. The distribution may be fit by a circular arc with radius $435 (\pm 7\%)$ mm. (—) The shape of the buckled, tethered membrane as determined by the optical profiler in the absence of applied voltage. b,c) Vertical displacement (Δh) at the center of the membrane with constant ± 5 V applied bias, as measured with an optical profiler, increased with time according to $\Delta h(t) = h_0(1 - e^{-t/\tau})$ giving characteristic response time of $\tau_{+5V} = 980 \pm 80$ s, $h_{0,+5V} = 2.95 \pm 0.08 \mu\text{m}$ and $\tau_{-5V} = 139 \pm 9$ s, and $h_{0,-5V} = 3.04 \pm 0.03 \mu\text{m}$. Only weak relaxation was observed during more than 2500 s following bias removal. d) Membrane charge/discharge cycle showing short circuit current of ≈ 62 nA when -5 V DC is removed after 380 s. e) Membrane charge/discharge cycle showing open circuit voltage of ≈ -0.25 V when -5 V DC is removed after 440 s. For measurements performed in (b–e), the bottom contact was at ground potential.

2.4. Optical Profiler Monitoring of Actuator Steady State

Given that SPM is sensitive to temperature fluctuations, we used an optical profiler to monitor the time required for the actuator to reach a steady state under DC bias of ± 5 V (Figure 3b–c, see Section 4, Experimental Section for instrument details). The steady state displacement (Δh_{ss}) at the center of the membrane was similar for both voltage directions ($|\Delta h_{ss}| \approx 3 \pm 0.2 \mu\text{m}$). However, under positive bias, the actuator displacement reached a plateau with time constant $\tau_+ = 980 \pm 80$ s, while under negative

bias, a plateau was achieved more rapidly, with time constant, $\tau_- = 139 \pm 9$ s. We suggest that the source of this difference in the steady state deformation time constant may lie in an as yet uncharacterized compositional or strain inequivalence of the WBs. Independent of bias polarity, when the DC bias is removed, the mechanical state of the actuator persists for ≈ 1 h. This persistence, even in the absence of applied voltage, provides support for our fundamental assertion that vertical displacement is due to mass transfer. Eventually, the actuator does revert to its initial state. We suggest that, in analogy to the self-discharge of a

battery, the fact that the actuator does not maintain its shape ad infinitum is due to electronic leakage current through the 20GDC electrolyte film. To buttress this suggestion, we monitored open circuit voltage (OCV) and short circuit current (SCC) with a low resistance multimeter after applying -5 V for 380 s (Figure 3d–e). SCC decayed in the course of 12 h (data not shown beyond 6 min) from $0.062 \mu\text{A}$ to zero, while the initial OCV of ≈ 0.25 V decays slowly as well. Given the high internal resistance of the ECM actuator to DC current (OCV/SCC ≈ 4 M Ω), this leakage allows oxygen ions to move through the IC electrolyte, thereby providing a “re-equilibrating” ion flux between the WBs.

2.5. Impedance Spectroscopy Measurements

Impedance spectroscopy (IS) was used to establish the presence of ionic diffusion and adequate total conductivity of the actuator. The Nyquist plot of the complex impedance (Z) of the membrane actuator at 354 mV, 1 MHz–4 mHz at room temperature (Figure 4a) comprises two readily discernable features: a depressed, high frequency arc and a constant phase element (CPE) at low frequencies. Between 3 and 785 Hz (46 data points), the arc may be fit to

$$\text{Im}(Z) = \gamma_0 + \left[R_0 - (\text{Re}(Z) - x_0)^2 \right]^n \quad (3)$$

with four parameters: $\gamma_0 = 226$ ($\pm 1.4\%$) k Ω , $x_0 = 693$ ($\pm 0.04\%$) k Ω , $R_0 = 771$ ($\pm 0.2\%$) k Ω , $n = 0.488$ ($\pm 0.03\%$) ($R_{\text{adj}}^2 = 0.99999$) (Figure 4a). Since $n \approx 0.5$, Equation (3) describes a circle with center at (x_0, γ_0) . Given that at room temperature, grain core and grain boundary impedance of 20GDC are not distinguishable,^[15] a combined equivalent RC circuit gives $R = 1.5$ M Ω and $C = 6.8$ nF. For a circular arc described by the Cole–Cole equation, the extent of the uniformity of the material relaxation may be estimated by $\alpha = 1 - \frac{2}{\pi} \tan^{-1} \left(\frac{\gamma_0}{x_0} \right)$ and related to the depression angle of $(1 - \alpha) \frac{\pi}{2}$ in the complex plane, where α characterizes a non-Debye like behavior.^[28] We find $\alpha \approx 0.8$ ($\alpha = 1$ defines a Debye semicircle) indicating reasonably homogeneous relaxation. The constant phase element (CPE) observed at frequencies < 50 mHz (Figure 4a) is a characteristic feature of diffusion-controlled electrode reactions. The slope of the CPE ($-\text{Im}(Z)/\text{Re}(Z)$) is $= 0.654$ ($\pm 0.8\%$), indicative of spatially restricted diffusion (for the unrestricted case, slope = 1).^[23,29]

2.6. Cyclic Voltammetry Measurements

The current–voltage characteristics of the membrane actuator, as determined by cyclic voltammetry at sufficiently low sweep rates, are also typical of ion-transport controlled devices. Room temperature scans, with rate 16–124 mV s^{-1} , are shown in Figure 4b. The voltammograms demonstrate that the current reaches a maximum both in the positive and negative potential ranges and the magnitudes of the current peaks, $|i_p|$, are linearly proportional to the square root of the sweep rate (ν) (Figure 4c). This behavior points to a reversible,

diffusion limited, electrochemical reaction as described by the Randles–Sevcik equation:^[23]

$$i_p = 0.446 \cdot n \cdot F \cdot A_c \cdot C \cdot \sqrt{\frac{z \cdot F \cdot \nu \cdot D}{RT}} \quad (4)$$

where $z = 2$ is the charge of the mobile species, n is the number of electrons transferred during oxidation/reduction, F is the Faraday constant, A_c is the contact area, D is the ion diffusion coefficient and C is the concentration of mobile species. The agreement with Equation (4) and the fact that the ratio between the positive and negative current peak amplitudes at each sweep rate is ≈ 1 , together suggest that the electrochemical reactions occurring in the WBs are quasi-reversible^[23,30] and are limited in the time domain by oxygen ion diffusion.

In analogy to a metal electrode immersed in an electrolyte solution, applying bias to the multilayer stack creates a diffuse layer in the electrolyte at the interface of the WB with the Ti metal electrode.^[23] Across the diffuse layer, potential drop is negligible and ions diffuse toward the electrode surface under the influence of their concentration gradient. On this basis, we conclude that oxygen transport in the WB layers is due to diffusion, rather than to electric field induced drift. Under quasi-static bias, the width of the diffuse layer becomes comparable to the measured thickness of the WB (see Section S6, Supporting Information). Assuming that the concentration of mobile species (oxygen vacancies) in the nanocomposite WB layers is similar to that in bulk 20GDC (≈ 0.016 mol cm^{-3}), the ion diffusion coefficient calculated with Equation (4) is $D_{\text{WB}} = (3.7 \pm 0.4) \cdot 10^{-15}$ $\text{cm}^2 \text{s}^{-1}$ (Figure 4c). This is more than an order of magnitude larger than that of bulk 20GDC at room temperature ($\approx 10^{-16}$ $\text{cm}^2 \text{s}^{-1}$).^[31,32] Such a significant increase in diffusion rate is indicative of rapid interfacial ion diffusion in the composite WBs, arising from the large surface area of the nanocrystalline structure^[33–36] (Figure S4b, Supporting Information) as compared to the bulk. The activation energy for oxygen diffusion calculated from the Arrhenius plot of the diffusion coefficient (Figure 4c, inset) in the temperature range 16–170 $^{\circ}\text{C}$ (Figure S5a–e, Supporting Information) is lower by $\approx 30\%$ as compared to published values for low temperature 20GDC.^[15,37]

2.7. Actuation Durability

To assess the long-term structural and functional integrity of the actuators at room temperature, they were subjected to multiple cycles of alternating voltage. The cyclic voltammograms acquired with sweep rate > 124 mV s^{-1} (3.2 mHz) show no significant change after thousands of cycles (Figure S6a, Supporting Information). Similarly, operating the actuators non-stop with 8 V at 50 mHz for 14 h does not alter subsequent response within the frequency range tested: 30 mHz–15 Hz (Figure S7a, Supporting Information). However, when the sweep rate is lowered to 31 mV s^{-1} (0.78 mHz), a change in the voltammograms is indeed observed. The voltammogram stabilizes after 100 cycles (≈ 35 h) but does not display any current peaks (Figure S6b, Supporting Information). Similarly, operating the actuators at 10 V, 0.78 mHz for > 100 cycles reduces the

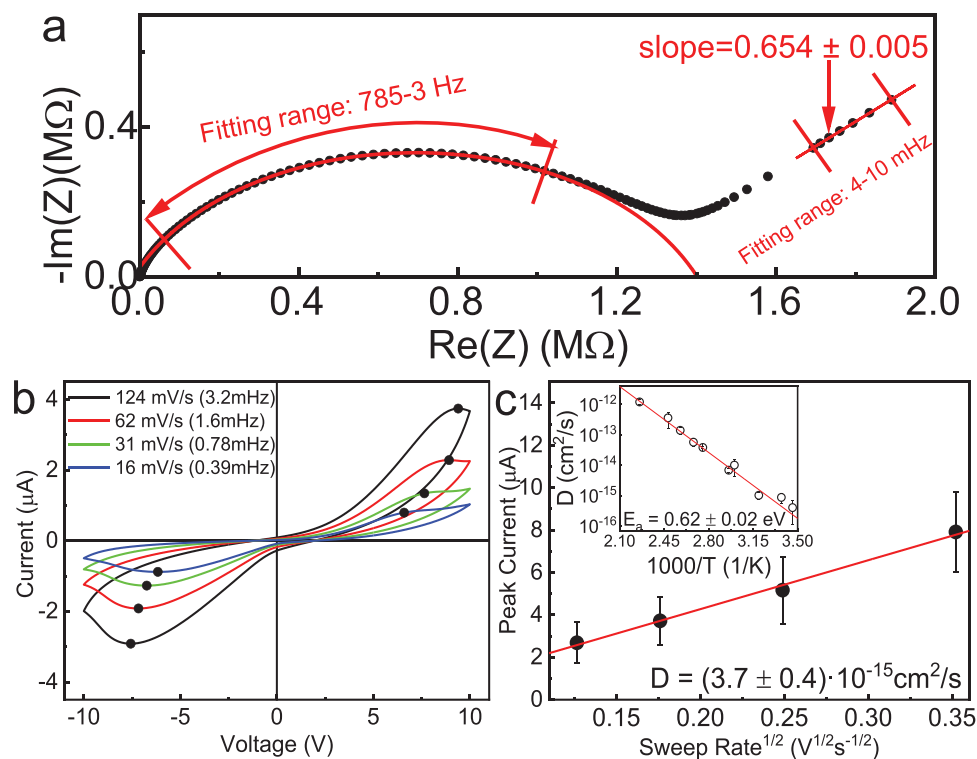


Figure 4. a) Nyquist plot of ECM actuator impedance at 354 mV excitation voltage, 1 MHz–4 MHz at room temperature. The high frequency arc can be fit to a depressed circle (radius R_0), centered at (x_0, y_0) in the complex plane: $-\text{Im}(Z) = y_0 + [R_0 \cdot (\text{Re}(Z) - x_0)^2]^n$ (Equation (3)) with $y_0 = 226 (\pm 1.4\%) \text{ k}\Omega$, $x_0 = 693 (\pm 0.04\%) \text{ k}\Omega$, $R_0 = 771 (\pm 0.2\%) \text{ k}\Omega$, $n = 0.488 (\pm 0.03\%)$, $R_{\text{adj}}^2 = 0.99999$. The slope of the low frequency constant phase element is: 0.654 ± 0.005 , $R_{\text{adj}}^2 = 0.9997$. b) Room temperature cyclic voltammetry measurements with sweep rates 16–124 mV s^{-1} , bottom contact at ground potential. Current peaks (I_p), indicating a reversible, diffusion limited, charge transfer process, were identified by double differentiation of the voltammogram and are indicated. c) Peak current as a function of the square root of the sweep rate, averaged over positive and negative applied voltage, for ten samples. The slope, determined by linear regression, is used to extract the diffusion coefficient according to the Randles–Sevcik equation (Equation (4)). Inset: Arrhenius plot of the ion diffusion coefficient between 16–170 °C averaged for seven samples. See Figure S5, Section S5, Supporting Information for temperature dependent cyclic voltammograms. Activation energy (E_a) for ion diffusion, $0.62 \pm 0.02 \text{ eV}$.

amplitude of the electromechanical response (Figure S7b, Supporting Information). A possible explanation for this behavior, based on the thickness of the nanocrystalline WBs and the oxygen diffusion coefficient, is outlined in Section S6, Supporting Information. Nevertheless, during two weeks at room temperature in the absence of bias, the mechanical response regains its original amplitude and current peaks in the cyclic voltammograms are again observed (Figure S7b and Figure S6b, Supporting Information).

3. Conclusion

In summary, we have demonstrated a room temperature, electro-chemo-mechanical (ECM) membrane actuator, with 20 mol% Gd doped ceria as the solid-state ion-conducting electrolyte. Comprising both charge transfer and oxygen ion diffusion, the mechanism governing the ECM response is fundamentally different from other actuation mechanisms in solids.^[1,2,38–40] The essential element of the actuator is the use of Ti oxide/20GDC nanocomposites as the WBs. The functional characteristics of the WBs are a) faster oxygen ion diffusion than is measured in the majority of mixed ionic/electronic conductors at room temperature; and b) the capability of

undergoing repeated oxidation/reduction reactions while preserving mechanical integrity. This allows the ECM actuator to achieve marked deformation within a short period of time. The actuator displays key features expected from an ECM device. It is mass-transport controlled and the buckled membrane temporarily retains its shape after DC voltage is removed. Our data indicate that ECM has the potential of becoming a practical actuation mechanism; the pseudo “piezoelectric” coefficient of the stacked layer membrane is estimated to be $>1.25 \text{ C m}^{-2}$ (see Section S7, Supporting Information), that is, comparable with lead-free piezoelectrics such as lithium niobate, sodium potassium niobate (KNN), or bismuth alkali.^[41] The response time of the actuator is limited by the diffusion coefficient of oxygen ions in the WBs; therefore, designing WBs with more rapid ion diffusion—e.g., with Li^+ or H^+ —is seen as a promising path for the creation of Si-integrated ECM MEMS.

4. Experimental Section

Sample Fabrication: Fabrication was carried out according to previously published protocols.^[16] Briefly, $\approx 150 \text{ nm}$ thick aluminum stress relief layer and a 300 nm thick titanium bottom contact were deposited at room temperature on a heavily p-doped Si wafer (100) in order to avoid Schottky barrier formation. The deposition process was accomplished

via DC magnetron sputtering (ATC Orion Series Sputtering System, AJA International Inc) from 2" metal targets (5 mTorr, 30 sccm Ar flow, power: 200 and 150 W on Al and Ti respectively). The ≈100 nm thick, bottom, Ti oxide/20GDC composite WB was co-sputtered by magnetron sputtering under reducing conditions (20 mTorr Ar; Ar flow: 30 sccm, power: Ti, 2" metallic target-DC, 150 W; 20GDC, 3" oxide target-RF, 100 W). ≈1.5 μm thick 20GDC solid electrolyte layer was deposited from a 3" oxide target with 1:10 O₂:Ar flow and 100 W. The upper WB and the top Ti/Al contact were then deposited as described above. Annealing was carried out in the sputtering chamber under vacuum at 430 °C for 4 h to promote stress relaxation. Top Ti/Al contact was patterned into a circular shape by lithography and wet metal etching. A 1 μm thick aluminum mask was then deposited on the backside of the Si wafer; circular holes were created in the mask by lithography and wet Al etch. Dry reactive ion etching (ICP STPS Technologies, KLA-Tencor) was used to etch the silicon through the circular holes in the aluminum mask, producing a self-supported, seven layer, tethered membrane, approximate thickness 2–2.5 μm. Finally, the wafer was cut into 8 × 8 mm² samples.

Microstructure Characterization: Characterization of the multilayer microstructure on Si was performed by scanning electron microscopy (SEM, Ultra, Carl Zeiss, 3 kV) and by a double aberration-corrected scanning transmission electron microscope (STEM, Thermo Fisher Scientific Microscopy Solutions, Themis-Z, 200 kV). A TEM sample was prepared by cutting a 100 nm thick slice from a sample cross section using a dual beam FIB-SEM instrument (FEI, Helios 600). Energy dispersive spectroscopy (EDS) hyperspectral data were obtained with a semi-convergence angle of 30 mrad at a beam current of 200 pA (FEI, windowless Super X detector). Quantitative elemental maps were calculated with Velox software (Thermo Fisher Scientific Electron Microscopy Solutions), including background subtraction and spectrum deconvolution. The scans included either the upper or lower WBs. Phase composition of the 20GDC electrolyte was determined by X-ray diffraction (Rigaku TTRAX III, Bragg Brentano, $\theta/2\theta$ mode, scan rate 2 ° min⁻¹). The strong (100) Si diffraction peak was avoided by performing the measurement with 3° offset. Average grain size in the WB composite was determined by the lineal intercept method applied to high resolution SEM micrographs of a composite layer deposited on fused SiO₂ with Al adhesion layer, and including the 1.56 multiplicative correction factor.^[42] 550 grains were counted. Morphology of the WB composite was determined by nano-beam electron diffraction (NBED) in STEM mode in a FEI Tecnai F20 Twin instrument (Thermo Fisher Scientific Microscopy Solutions) with a semi-convergence angle of 0.4 rad and a probe size of 10 nm (Gatan, Orius SC600A CCD).

Optical Profiling: An optical profiler (Zeta-20, Zeta Instruments, KLA-Tencor) was used to examine the buckling shape, to verify absence of micro-cracks in the self-supported devices and to measure the mechanical response of the device to DC bias. A ×20 magnification objective was used for visual inspection scanning, a 7 × 5 matrix of 306 × 447 μm² images was recorded with 10% overlap, obtaining a 2143 × 2236 μm² 3D profile. To measure displacement as a function of time under DC bias, a 700 × 524 μm² frame from the center of the self-supported structure was scanned continuously with a ×20 magnification objective at 5–6 min intervals. To measure the change in the shape of the self-supported film stack, five frames of 205 × 35 μm² from the central 1 mm of the tethered membrane were acquired with a ×50 magnification objective and were then spliced together to produce a 2D profile. ≈30 min of –5V bias were applied and the resulting profile was compared to the initial state. The profiles were smoothed using a Savitzky–Golay filter with a 300-point window, followed by second order polynomial fitting. The radius of curvature of the central 1 mm was extracted using a circular function fit accomplished with the direct least squares fitting algorithm in MatLab.

Electrical Characterization: Electrical characterization of the membrane actuator was performed with cyclic voltammetry (CV) (B2912A Precision Source/Measure Unit, Keysight Technology Inc, internal ammeter resistance <200 Ω) and impedance spectroscopy (IS) (ZG-4 with Alpha-A modular measurement system, Novocontrol Technologies GmbH and Co. KG) with voltage applied between top and bottom

Al/Ti contacts. Ten samples were measured under ambient conditions by CV and seven samples were measured as a function of temperature. Temperature dependent CV in the range of 16–170 °C was performed using a heating resistor connected to an auto-tuning temperature controller (321, Lakeshore, PT100 thermometer). Seven samples were measured by IS under ambient conditions. In order to identify remanent current and voltage, measurements were performed using a high precision electrometer (6514, Keithley, internal resistance 200 TΩ) on three samples during charging/discharging.

Electromechanical Characterization: Electromechanical characterization was performed with scanning probe microscopy (SPM, NTEGRA, SMENA head, NT-MDT Spectrum Instruments) under ambient conditions. In this instrument, Z position of the piezo is monitored by a calibrated sensor. Semi-contact mode was used, in which an oscillating tip (AC160, Olympus, with nominal force constant 40 Nm⁻¹) tracks the position of the upper contact under feedback control. To avoid electrostatic artifacts, the SPM tip and the top electrode were electrically grounded, while voltage was supplied to the bottom contact with a function generator (Rigol, DG4062). Six samples were tested and their response averaged.

X-Ray Absorption Measurements: XANES measurements were made on beamline 7-BM, National Synchrotron Light Source II, Brookhaven National Laboratory. Both Ti K-edge and Ce L₃-edge data were collected in fluorescence mode (See Section S1, Supporting Information for XANES spectra).

Data Processing and Analysis: The amplitude of the ECM response was extracted by identifying positive and negative peaks in the SPM sensor height data; peak-to-peak difference was averaged and divided by two. All non-linear function fitting procedures were accomplished by OriginLab Pro.

Supporting Information

Supporting Information is available from the Wiley Online Library or from the author.

Acknowledgements

This work was supported in part by the BioWings project, which has received funding from the European Union's Horizon 2020 under the Future and Emerging Technologies (FET) program with grant agreement No. 801267. I.L. and A.I.F. acknowledge the NSF-BSF program grant 2018717. A.I.F., Y.L., and J.L. acknowledge support by NSF Grant number DMR-1911592. This research used beamline 7-BM (QAS) of the National Synchrotron Light Source II, a U.S. DOE Office of Science User Facility operated for the DOE Office of Science by Brookhaven National Laboratory (BNL) under Contract No. DE-SC0012704. IL and E.M. acknowledge Mrs. Katya Rechav for TEM lamellar sample preparation and Mr. Ilya Makagon for graphical design of Figure 1. This research is made possible in part by the historic generosity of the Harold Perlman Family.

Conflict of Interest

The authors declare no conflict of interest.

Keywords

actuation, chemo-mechanics, micro-electro-mechanical systems, oxygen-ion conductors

Received: August 9, 2020

Revised: September 18, 2020

Published online: October 7, 2020

- [1] L. E. Cross, W. Heywang, *Piezoelectricity: Evolution and Future of a Technology*, Springer Series in Materials Science, Vol. 114, Springer-Verlag, Berlin **2008**, p. 1.
- [2] R. Yimnirun, P. J. Moses, R. E. Newnham, R. J. Meyer, *J. Electroceram.* **2002**, *8*, 87.
- [3] N. Setter, D. Damjanovic, L. Eng, G. Fox, S. Gevorgian, S. Hong, A. Kingon, H. Kohlstedt, N. Y. Park, G. B. Stephenson, I. Stolitchnov, A. K. Tagantsev, D. V. Taylor, T. Yamada, S. Streiffner, *J. Appl. Phys.* **2006**, *100*, 051606.
- [4] A. Kholkin, *Ferroelectrics* **2001**, *258*, 209.
- [5] J. G. Swallow, J. J. Kim, J. M. Maloney, D. Chen, J. F. Smith, S. R. Bishop, H. L. Tuller, K. J. Van Vliet, *Nat. Mater.* **2017**, *16*, 749.
- [6] S. R. Bishop, N. H. Perry, D. Marrocchelli, B. W. Sheldon, *Electro-Chemo-Mechanics of Solids*, Springer International Publishing, New York **2017**.
- [7] J. G. Swallow, W. H. Woodford, Y. Chen, Q. Lu, J. J. Kim, D. Chen, Y. M. Chiang, W. C. Carter, B. Yildiz, H. L. Tuller, K. J. Van Vliet, *J. Electroceram.* **2014**, *32*, 3.
- [8] S. R. Bishop, D. Chen, Y. Kuru, J. J. Kim, T. S. Stefanik, H. L. Tuller, *ECS Trans.* **2011**, *33*, 51.
- [9] S. R. Bishop, D. Marrocchelli, C. Chatzichristodoulou, N. H. Perry, M. B. Mogensen, H. L. Tuller, E. D. Wachsman, *Annu. Rev. Mater. Res.* **2014**, *44*, 205.
- [10] K. Amine, R. Kanno, Y. H. Tzeng, *MRS Bull.* **2014**, *39*, 395.
- [11] J. D. Nicholas, Y. Qi, S. R. Bishop, P. P. Mukherjee, *J. Electrochem. Soc.* **2014**, *161*, Y11.
- [12] X. J. Wang, F. F. Fan, J. W. Wang, H. R. Wang, S. Y. Tao, A. Yang, Y. Liu, H. B. Chew, S. X. Mao, T. Zhu, S. M. Xia, *Nat. Commun.* **2015**, *6*, 8417.
- [13] S. Golmon, K. Maute, S. H. Lee, M. L. Dunn, *Appl. Phys. Lett.* **2010**, *97*, 033111.
- [14] V. A. Sethuraman, M. J. Chon, M. Shimshak, V. Srinivasan, P. R. Guduru, *J. Power Sources* **2010**, *195*, 5062.
- [15] E. Mishuk, A. Ushakov, E. Makagon, S. R. Cohen, E. Wachtel, T. Paul, Y. Tsur, V. Y. Shur, A. Kholkin, I. Lubomirsky, *Adv. Mater. Interfaces* **2019**, *6*, 1801592.
- [16] E. Mishuk, E. Makagon, E. Wachtel, S. R. Cohen, R. Popovitz-Biro, I. Lubomirsky, *Sensor Actuat. A* **2017**, *264*, 333.
- [17] O. Kraynis, E. Makagon, E. Mishuk, M. Hartstein, E. Wachtel, I. Lubomirsky, T. Livneh, *Adv. Func. Mater.* **2019**, *29*, 1804433.
- [18] S. P. Jiang, S. H. Chan, *J. Mater. Sci.* **2004**, *39*, 4405.
- [19] N. H. Menzler, F. Tietz, S. Uhlenbruck, H. P. Buchkremer, D. Stover, *J. Mater. Sci.* **2010**, *45*, 3109.
- [20] P. I. Cowin, C. T. G. Petit, R. Lan, J. T. S. Irvine, S. W. Tao, *Adv. Energy. Mater.* **2011**, *1*, 314.
- [21] L. Kong, D. J. Gregg, E. R. Vance, I. Karatchevtseva, G. R. Lumpkin, M. G. Blackford, R. Holmes, M. Jovanovic, G. Triani, *J. Eur. Ceram. Soc.* **2017**, *37*, 2179.
- [22] V. Vales, L. Matejova, Z. Matej, T. Brunatova, V. Holy, *J. Phys. Chem. Solids* **2014**, *75*, 265.
- [23] A. J. Bard, L. R. Faulkner, J. Leddy, C. G. Zoski, *Electrochemical Methods: Fundamentals and Applications*, Wiley, New York **1980**.
- [24] R. Korobko, A. Patlolla, A. Kosoy, E. Wachtel, H. L. Tuller, A. I. Frenkel, I. Lubomirsky, *Adv. Mater.* **2012**, *24*, 5857.
- [25] N. Yavo, O. Yeheskel, E. Wachtel, D. Ehre, A. I. Frenkel, I. Lubomirsky, *Acta Mater.* **2018**, *144*, 411.
- [26] M. Varenik, S. Cohen, E. Wachtel, A. I. Frenkel, J. C. Nino, I. Lubomirsky, *Scr. Mater.* **2019**, *163*, 19.
- [27] S. P. Timoshenko, *Theory of Elasticity*, McGraw-Hill, New York **1987**.
- [28] I. Bunget, M. Popescu, *Physics of Solid Dielectrics*, Elsevier, New York **1984**.
- [29] V. F. Lvovich, *Impedance Spectroscopy: Applications to Electrochemical and Dielectric Phenomena*, Wiley, New York **2015**.
- [30] N. Elgrishi, K. J. Rountree, B. D. McCarthy, E. S. Rountree, T. T. Eisenhart, J. L. Dempsey, *J. Chem. Educ.* **2018**, *95*, 197.
- [31] S. Kazlauskas, A. Kezionis, T. Salkus, A. F. Orliukas, *J. Mater. Sci.* **2015**, *50*, 3246.
- [32] H. Inaba, H. Tagawa, *Solid State Ionics* **1996**, *83*, 1.
- [33] N. Sata, K. Eberman, K. Eberl, J. Maier, *Nature* **2000**, *408*, 946.
- [34] P. Heitjans, S. Indris, *J. Phys.* **2003**, *15*, R1257.
- [35] J. Garcia-Barriocanal, A. Rivera-Calzada, M. Varela, Z. Sefrioui, E. Iborra, C. Leon, S. J. Pennycook, J. Santamaria, *Science* **2008**, *321*, 676.
- [36] S. Kim, J. S. Lee, C. Mitterbauer, Q. M. Ramasse, M. C. Sarahan, N. D. Browning, H. J. Park, *Chem. Mater.* **2009**, *21*, 1182.
- [37] G. Lazovski, O. Kraynis, R. Korobko, E. Wachtel, I. Lubomirsky, *Solid State Ionics* **2015**, *277*, 30.
- [38] *Piezoelectricity: Evolution and Future of a Technology*, Springer Series in Materials Science, (Eds: W. Heywang, K. Lubitz, W. Wersing), Vol. 114, Springer-Verlag, Berlin **2008**.
- [39] R. E. Newnham, V. Sundar, R. Yimnirun, J. Su, Q. M. Zhang, *Ceram. Trans.* **1998**, *88*, 15.
- [40] X. Zhao, Q. Wang, *Appl. Phys. Rev.* **2014**, *1*, 021304.
- [41] J. Rodel, W. Jo, K. T. P. Seifert, E. M. Anton, T. Granzow, D. Damjanovic, *J. Am. Ceram. Soc.* **2009**, *92*, 1153.
- [42] M. I. Mendelson, *J. Am. Ceram. Soc.* **1969**, *52*, 443.